NENE
International Conference
Nuclear Energy for New Europe

ANALYSIS OF STRAIN LOCALIZATION IN IRRADIATED AUSTENITIC STAINLESS STEELS USING FFT-BASED CRYSTAL PLASTICITY SIMULATIONS

Amirhossein Lame Jouybari[a,b]
[a]Jožef Stefan Institute
Jamova cesta 39
SI-1000, Ljubljana, Slovenia
amirhossein.lame@ijs.si

Samir El Shawish[a], Leon Cizelj[a,b]
[b]University of Ljubljana
Jadranska ulica 19
SI-1000, Ljubljana, Slovenia
samir.elshawish@ijs.si, leon.cizelj@ijs.si

ABSTRACT

The harsh environment of Light Water Reactors (LWR) deteriorates the mechanical properties of internal structures within the reactor. Austenitic stainless steels are among the best structural materials to operate in the LWR environment due to their excellent mechanical properties, and high resistance to stress-corrosion cracking and irradiation damage. However, extended use of these steels may give rise to a unique deformation mode characterized by localized strain in terms of slip and kink bands (also known as clear channels). Such strain localization may lead to a premature strength reduction of the internal components.

The Fast Fourier Transform (FFT) method for the homogenization of composites under periodic boundary conditions is based on the discretized Lippmann-Schwinger equation and Fourier series, and was first developed in 1998. Since then, this method has been extended to polarization-based methods, Krylov approaches, Fourier–Galerkin, and displacement-based methods and pushed beyond a variety of studies containing multi-scale modeling, multi-physics problem, crystal plasticity, etc.

This paper proposes a novel FFT algorithm in the framework of crystal plasticity in terms of modified Green operator and Anderson acceleration to acquire the converged displacement and stress fields of irradiated polycrystals under tensile loading. Furthermore, the algorithm employs special indicators to identify regions of strain localization within the polycrystalline aggregate, and distinguishes kink bands from slip bands by carefully analyzing crystal lattice rotations.

1 INTRODUCTION

Nuclear power, a promising and environmentally friendly energy source, has nonetheless faced challenges. These have manifested as the revelation of potential vulnerabilities in the structural integrity of reactor components. Addressing these concerns requires a robust understanding of material science and fracture mechanics, pivotal elements that hold the key to enhancing structural safety and ensuring a secure trajectory for the future of nuclear technology.

Austenitic stainless steel alloys find extensive application in the design of nuclear reactor internals. These alloys are prone to the development of defects in their microstructure due to the presence of neutrons and subsequent ballistic interactions with steel atoms, resulting in diminished strength, ductility, and altered fracture behavior compared to typical (unirradiated) conditions. Previous experimental findings have shown that irradiation leads to increased heterogeneity in the deformation mode, resulting in intense deformation within narrow channels [1]. These channels, widely recognized as ”clear channels”, emerge due to the high density of dislocation gliding in these regions, effectively sweeping away hardening defects. This phenomenon results in material softening, reduced alloy lifespan, and eventual failure. Clear channels are commonly categorized into two types: slip bands (aligned parallel to slip planes) and kink bands (rotated in relation to slip planes). This study endeavors to establish a systematic framework for distinguishing between various types of clear channels.

Fast Fourier transform (FFT) homogenization method operates by resolving the Cauchy equilibrium equation of motion through the convolution between the source of heterogeneity and the Green operator. The inherent periodicity of tensors, along with advantages such as reduced memory allocation, direct utilization of microstructural images without the need for meshing, and a lower computational burden compared to the finite element method, render the FFT method a formidable contender in this domain.

In this paper, the theoretical background of crystal plasticity and Lippmann-Schwinger equation is outlined in Section 2. The pseudo code of the FFT-based method is described in Section 3. The results are discussed in Section 4 in terms of the macroscopic mechanical behavior of austenitic stainless steel and corresponding localization band detection. Section 5 provides the conclusions. The notation used in this paper is outlined in Appendix A.1.

2 CRYSTAL PLASTICITY AND LIPPMANN-SCHWINGER EQUATION

On a microscale, the atoms of austenitic stainless steel alloys periodically arrange into Face Centered Cubic crystal lattice. Within this structure, dislocations glide along 12 specific pathways known as slip systems indicated by Miller indices as $\{111\}\langle 110\rangle$. The mechanical theory of crystal deformation is based on the concept that dislocations initiate their motion along active slip systems, succeeded by the subsequent overlay of elastic distortion. This study attempts to simulate the elasto-viscoplastic behavior of irradiated polycrystals on the microscale that have been implemented in the Matlab code [2].

In the small strain framework of crystal plasticity, the total deformation gradient additively decomposes into the elastic and plastic parts of the displacement gradient tensor (Eqs. (1), (2)) [3]. This leads to a set of corresponding constitutive equations[1] encompassing linear elastic behavior between stresses (Eq. (4)) and strains (Eq. (3)), resolved shear stress (Eq. (5)), plastic flow rule (Eq. (6)), and critical resolved shear stress (Eq. (7)). Notably, the critical resolved shear stress incorporates an exponential softening, which captures the effects of both irradiation-induced hardening and dislocation glide-driven defect removal [3].

$$\underset{\sim}{F} = \underset{\sim}{1} + \nabla \underline{u}^{\mathsf{e}} + \nabla \underline{u}^{\mathsf{p}} \tag{1}$$

$$\underset{\sim}{F}^{\mathsf{e}} = \underset{\sim}{1} + \nabla \underline{u}^{\mathsf{e}} \tag{2}$$

$$\underset{\sim}{\varepsilon}^{\mathsf{e}} = \mathsf{sym}(\nabla \underline{u}^{\mathsf{e}}) = \tfrac{1}{2}(\nabla \underline{u}^{\mathsf{e}} + \nabla \underline{u}^{\mathsf{e}^{\mathsf{T}}}) \tag{3}$$

$$\underset{\sim}{\sigma} = \underset{\approx}{\Lambda} : \underset{\sim}{\varepsilon}^{\mathsf{e}} \tag{4}$$

$$\tau^{\mathsf{s}} = \underset{\sim}{\sigma} : \mathsf{sym}(\underset{\sim}{\mu}^{\mathsf{s}}) \tag{5}$$

[1] Details of time integration are given in Appendix A.2.

$$\dot{\gamma}^{\mathsf{s}} = \mathsf{sign}(\tau^{\mathsf{s}}) \left\langle \frac{\left|\tau^{\mathsf{s}}\right| - \tau^{\mathsf{s}}_{\mathsf{cr}}}{k} \right\rangle^{\mathsf{n}} \tag{6}$$

$$\tau^{\mathsf{s}}_{\mathsf{cr}} = \tau^{\mathsf{s}}_{0} - \Delta\tau \left[1 - \exp\left(-\frac{\gamma^{\mathsf{s}}_{\mathsf{cum}}}{\gamma^{\mathsf{s}}_{0}}\right)\right] + \mathsf{H}^{\mathsf{s}}\gamma^{\mathsf{s}}_{\mathsf{cum}} \tag{7}$$

$$\gamma^{\mathsf{s}}_{\mathsf{cum}} = \int_0^t \left|\dot{\gamma}^{\mathsf{s}}\right| dt \tag{8}$$

The *Lippmann-Schwinger* equation [4] is derived by the additive decomposition of the total displacement gradient tensor into the fluctuation and average terms, assuming the fluctuation term is periodic and the traction vector is anti-periodic on the boundary of material ($\partial\mathcal{B}$). Additionally, an auxiliary homogeneous isotropic linear elastic material with the elasticity tensor $\underset{\approx}{\Lambda}^{\mathsf{h}}$ is introduced to define the polarization tensor.

$$\begin{cases} \nabla\underline{u}^{\mathsf{tot}}(\underline{x}) = \overline{\nabla\underline{u}} + \nabla\underline{u}^{\star}(\underline{x}) & \forall\underline{x} \in \mathcal{B}, \;\; \nabla\underline{u}^{\star}\#\partial\mathcal{B} \\ \underset{\sim}{\sigma}(\underline{x}) = \underset{\approx}{\Lambda}(\underline{x}) : \mathsf{sym}(\nabla\underline{u}^{\mathsf{e}}) & \forall\underline{x} \in \mathcal{B}, \;\; \underset{\sim}{\sigma}.\underline{n} - \#\partial\mathcal{B} \\ \underset{\sim}{\tau}(\underline{x}) = \underset{\sim}{\sigma}(\underline{x}) - \underset{\approx}{\Lambda}^{\mathsf{h}} : \mathsf{sym}(\nabla\underline{u}^{\mathsf{tot}}(\underline{x})) & \forall\underline{x} \in \mathcal{B} \\ \mathsf{div}\left(\underset{\sim}{\sigma}(\underline{x})\right) = \underline{0} & \forall\underline{x} \in \mathcal{B} \end{cases} \tag{9}$$

The solution in real space and Fourier space is obtained by applying a Green operator ($\underset{\approx}{\Gamma}^{\mathsf{M}}$):

Real space: $$\nabla\underline{u}^{\mathsf{tot}}(\underline{x}) = -\underset{\approx}{\Gamma}^{\mathsf{M}} * \underset{\sim}{\tau}(\underline{x}) \tag{10}$$

Fourier space: $$\begin{cases} \widehat{\nabla\underline{u}}^{\mathsf{tot}}(\underline{\xi}) = -\underset{\approx}{\widehat{\Gamma}}^{\mathsf{M}}(\xi) : \underset{\sim}{\widehat{\tau}}(\underline{\xi}) & \forall\underline{\xi} \neq \underline{0} \\ \widehat{\nabla\underline{u}}^{\mathsf{tot}}(\underline{0}) = \overline{\nabla\underline{u}} \end{cases} \tag{11}$$

A significant advantage of computing in the Fourier space is that the convolution integral operator in real space (Eq. (10)) simplifies into double contraction in Fourier space (Eq. (11)), which results in reduced computational cost.

2.1 Localization band detection

The aforementioned crystal plasticity framework presented in the previous section enables us to distinguish the plastic strain localization regions in the material by introducing new variables as effective cumulative plastic deformation, p, and rotation angle θ[2][3].

$$p = \int_0^t \sqrt{\sum_s \dot{\gamma}^{\mathsf{s}}\underset{\sim}{\mu}^{\mathsf{s}} : \sum_s \dot{\gamma}^{\mathsf{s}}\underset{\sim}{\mu}^{\mathsf{s}}}\, dt \tag{12}$$

$$\theta = \arccos\left(\frac{1}{2}\left(\mathsf{tr}\left[\underset{\sim}{R}^{\mathsf{e}}\right] - 1\right)\right) \tag{13}$$

Two Heaviside functions, defined by thresholds based on the mean values ($\bar{p},\ \bar{\theta}$) and user-defined factors ($\Phi_L,\ \Phi_R$), have been formulated to detect regions of slip localization and high lattice rotation.

$$\mathcal{L}(\underline{X}) = \mathcal{H}\left(p(\underline{X}) - \bar{p}\Phi_L\right) \tag{14}$$

$$\mathcal{R}(\underline{X}) = \mathcal{H}\left(\theta(\underline{X}) - \bar{\theta}\Phi_R\right) \tag{15}$$

The following indicator functions are considered to explicitly detect slip and kink bands,

$$\mathcal{K}(\underline{X}) = \mathcal{L}(\underline{X}) \times \mathcal{R}(\underline{X}) \tag{16}$$

$$\mathcal{S}(\underline{X}) = \mathcal{L}(\underline{X}) - \mathcal{K}(\underline{X}) \tag{17}$$

[2]The rotation tensor is obtained by polar decomposition of the elastic part of deformation gradient ($\underset{\sim}{F}^{\mathsf{e}} = \underset{\sim}{R}^{\mathsf{e}}.\underset{\sim}{U}^{\mathsf{e}}$).

In this formulation, localization bands are recognized as kink bands (high strain localization and high lattice rotation) if $\mathcal{K}(\underline{X}) = 1$, and slip bands (high strain localization and small lattice rotation) if $\mathcal{S}(\underline{X}) = 1$.

Table 1: Pseudo code of the FFT-Algorithm

1	Extrapolation of the total displacement gradient tensor field at zero-FFT iteration $\nabla \underline{u}^{\text{tot,i}}(t_n + \Delta t_n) = \nabla \underline{u}^{\text{tot}}(t_n) + \frac{\Delta t_n}{\Delta t_{n-1}}(\nabla \underline{u}^{\text{tot}}(t_n) - \nabla \underline{u}^{\text{tot}}(t_{n-1}))$
2	Implicit time integration of state variables at zero iteration ($i == 0$) $\underset{\sim}{\varepsilon}^{e,i}(t_n + \Delta t_n),\ \underset{\sim}{\sigma}^{\text{i}}(t_n + \Delta t_n),\ \gamma^{\text{s,i}}(t_n + \Delta t_n)$
3	New Iteration FFT-loop ($i = i + 1$)
4	Cauchy equilibrium convergence test $\text{error}^i_{\text{Cauchy}} = \frac{\left(\frac{1}{N^{\text{tot}}} \sum_d ||\underline{\text{f}}'_d \cdot \underset{\sim}{\widehat{\sigma}}^{\text{i-1}}(\underline{\xi}_d)||^2\right)^{1/2}}{||\underset{\sim}{\widehat{\sigma}}^{\text{i-1}}(\underline{0})||} < \text{Tol}_{\text{Cauchy}}$
5	Evaluating polarization field $\underset{\sim}{\tau}^{\text{i}} = \underset{\sim}{\sigma}^{i-1} - \underset{\approx}{\Lambda}^h : \nabla \underline{u}^{\text{tot,i-1}}$
6	Transferring polarization tensor to Fourier space $\underset{\sim}{\widehat{\tau}}^{\text{i}}(\underline{\xi}) = \mathcal{FFT}\left(\underset{\sim}{\tau}^{\text{i}}\right)$
7 7.1 7.2	Mixed boundary condition: tensile loading Evaluating loading parameter $k^{\text{i}} = \frac{\overline{\nabla \underline{u}}^{\text{tot,i-1}} : \underset{\sim}{\Sigma}^0 + \underset{\sim}{\Sigma}^0 : \left(\left[\underset{\approx}{\Lambda}^h\right]^{-1} : \underset{\sim}{\bar{\sigma}}^{i-1} - \overline{\nabla \underline{u}}^{\text{tot,i-1}}\right)}{\underset{\sim}{\Sigma}^0 : \left[\underset{\approx}{\Lambda}^h\right]^{-1} : \underset{\sim}{\Sigma}^0}$ Evaluating macroscopic displacement gradient tensor field $\overline{\nabla \underline{u}}^{\text{tot,i}} = \overline{\nabla \underline{u}}^{\text{tot,i-1}} + \left[\underset{\approx}{\Lambda}^h\right]^{-1} : \left(k^{\text{i}} \underset{\sim}{\Sigma}^0 - \underset{\sim}{\bar{\sigma}}^{i-1}\right)$
8	Evaluating displacement gradient tensor field by Green operator in Fourier space $\widehat{\nabla \underline{u}}^{\text{tot,i}}(\underline{\xi}) = -\underset{\approx}{\widehat{\Gamma}}^{\text{M}}(\xi) : \underset{\sim}{\widehat{\tau}}^i(\underline{\xi}) \qquad \forall \underline{\xi} \neq \underline{0}$ $\widehat{\nabla \underline{u}}^{\text{tot,i}}(\underline{0}) = \overline{\nabla \underline{u}}^{\text{tot,i}}$
9	Returning displacement gradient tensor field to real space $\nabla \underline{u}^{\text{tot,i}}(\underline{X}) = \mathcal{IFFT}\left(\widehat{\nabla \underline{u}}^{\text{tot,i}}(\underline{\xi})\right)$
10 10.1 10.2	Anderson Acceleration Saved displacement gradient tensor field at current iteration. Apply if ($i/3 == 3k, \quad k = 1, 2, 3, ...$)
11	Implicit time integration of state variables at current iteration $\underset{\sim}{\varepsilon}^{e,i}(t_n + \Delta t_n),\ \underset{\sim}{\sigma}^{\text{i}}(t_n + \Delta t_n),\ \gamma^{\text{s,i}}(t_n + \Delta t_n)$
12	Localization detection
13 13.1 13.2	Convergence tests: mixed boundary conditions Stress macroscopic on non-tensile directions $\text{error}^i_{\text{Stress Mac}} = \frac{||\underset{\sim}{\bar{\sigma}}^{\text{i}}(\underline{0}) - k^{\text{i}} \underset{\sim}{\Sigma}^0||}{||k^{\text{i}} \underset{\sim}{\Sigma}^0||} < \text{Tol}_{\text{Stress Mac}} \quad \{\forall ij \mid \sigma_{ij} = \text{tensile direction}\}$ Strain macroscopic on tensile direction $\text{error}^i_{\text{Strain Mac}} = \frac{||\widehat{\nabla \underline{u}}^{\text{i}}(\underline{0}) - \overline{\nabla \underline{u}}||}{||\widehat{\nabla \underline{u}}^{\text{i}}(\underline{0})||} < \text{Tol}_{\text{Strain Mac}} \quad \{\forall ij \mid \varepsilon_{ij} \neq \text{tensile direction}\}$
14 14.1 14.2	If all convergence tests satisfied the tolerances Yes: Updating time No: Go to step 3.

3 FFT-BASED COMPUTATIONAL ALGORITHM

The process of finding the displacement gradient involves employing a fixed point (*Picart*) iteration that converges linearly to the desired solution. To expedite this process, (i) a specific variant of *Anderson acceleration*, known as Altered $2 - \delta$ method [5], and (ii) a modified Green operator (Eq. (18)) are established to enhance the accuracy of local field resolution [6].

$$\underset{\approx}{\widehat{\Gamma}}^{\text{M}} = \underline{\text{f}} \otimes \left[\underline{\text{f}} \cdot \underset{\approx}{\Lambda}^{\text{h}} \cdot \underline{\text{f}}'\right]^{-1} \otimes \underline{\text{f}}' \tag{18}$$

$$\mathfrak{f}_j = \mathrm{i}\sin\left(\xi_j\right) \tag{19}$$

$$\mathfrak{f}'_j = \mathrm{i}\mathfrak{f}_j \tag{20}$$

$$\xi_i = \frac{2\pi m_i}{L_i}, \quad m_i = 1-(N_i/2), 2-(N_i/2), ..., 0, ..., (N_i/2)-1, (N_i/2) \tag{21}$$

The overall structure of the proposed FFT-Algorithm is given in Table 1.

4 RESULTS

The FFT-based homogenization method is used to simulate the tensile loading of two different polycrystalline models (Voronoi tessellation), a 5-grain aggregate discretized by 64^3 voxels, and a 16-grain aggregate discretized by 90^3 voxels [7]. Tensile loading is applied by assigning mixed boundary conditions. In this respect, the displacement gradient tensor is prescribed on the Z-direction to simulate a strain rate of 10^{-5} s^{-1} and a zero mean value for Cauchy stress tensor is specified for other directions. The material properties used in the simulations are given in Table 2.

Table 2: Two sets of material properties

State	K	n	E	ν	τ_0^s	$\Delta\tau$	γ_0^s	H^s
Irradiated	10 MPa s^{-n}	15	100 GPa	0.3	100 MPa	20 MPa	0.1	0 MPa
UnIrradiated	10 MPa s^{-n}	15	100 GPa	0.3	100 MPa	0 MPa	0.1	40 MPa

Figure 1 represents the calculated tensile responses of both aggregates for two sets of material parameters. A typical elasto-viscoplastic behavior is observed with identical elastic responses and common yield stress. Note that the observed macroscopic softening (blue and violet curves in Fig. 1) is typical for irradiated austenitic stainless steel.

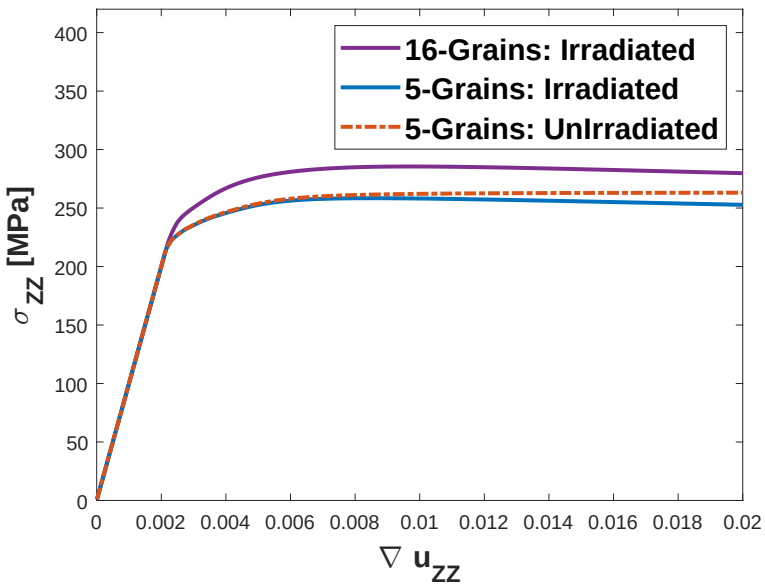

Figure 1: Macroscopic tensile curves for different aggregate sizes and material properties.

Figure 2 demonstrates the distribution of the total cumulative shear strain ($\sum_s \gamma^s_{\text{cum}}$) and slip and kink band distributions within the 16-grain aggregate model at final deformation ($\nabla u_{ZZ} = 0.02$). The results show that plastic deformation due to dislocations glide is localized within narrow bands (usually only one or two voxels wide). This kind of plastic localization, appearing at relatively small tensile strain ($\sim 2\%$), has been also observed experimentally in irradiated austenitic stainless steels [1]. It is believed that the interaction of such localization bands

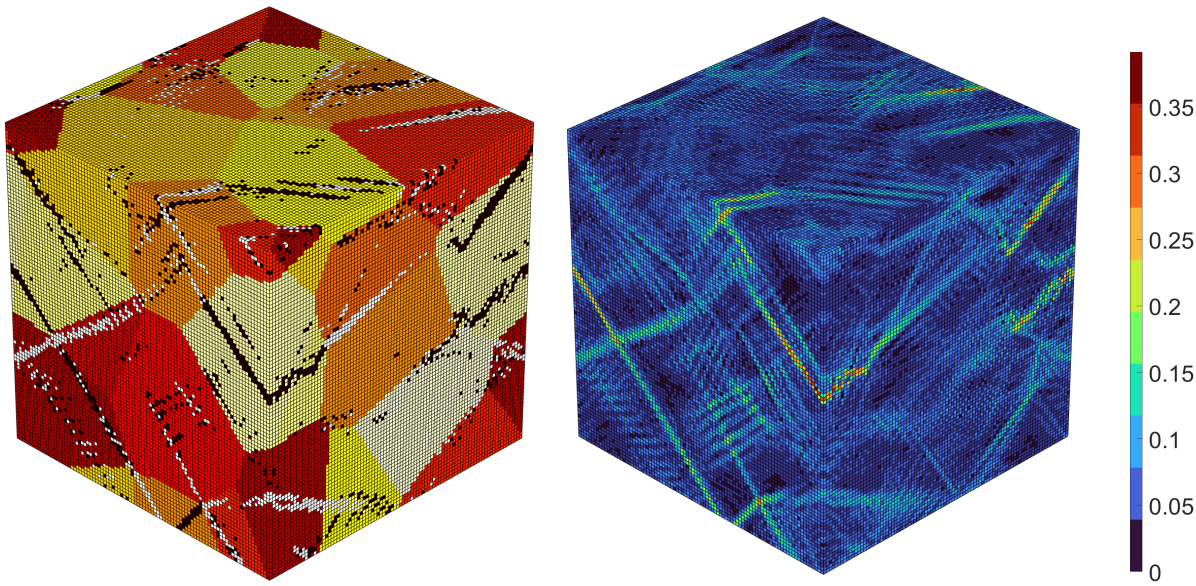

Figure 2: 16-grain aggregate (with 90^3 voxels) at $\nabla u_{ZZ} = 0.02$.
Left: slip bands (black lines) and kink bands (white lines). Right: total cumulative shear strain $(\sum_s \gamma^{\mathsf{s}}_{\mathsf{cum}})$

with grain boundaries is crucial for the initiation of micro cracks when the material is additionally exposed to the corrosive environment (e.g., Irradiation-Assisted Stress Corrosion Cracking (IASCC) [8]). Moreover, the visualization of individual grains allows us to observe different qualitative aspects of the localization behavior. Namely, the localization bands may stop at grain boundaries, or they may extend across several grains (with a possible slip/kink band type transition), or they can disappear or change a direction within a grain. It also seems that many of the localization bands intersect (or pass very closely to) the grain triple points. This may indicate that triple points are indeed the initiators of the localization bands.

5 CONCLUSIONS

A novel FFT-based homogenization method in the framework of crystal plasticity has been proposed and computationally implemented in the Matlab software. When applied to polycrystalline models of irradiated austenitic stainless steel, the method has correctly predicted the macroscopic softening response, which microscopically corresponds to the formation of so-called clear channels. These localization bands have been distinguished into slip and kink bands, depending on their inclination with respect to slip planes. The simulations have additionally revealed that the formation of bands is potentially influenced by the proximity to grains triple points.

ACKNOWLEDGMENTS

The authors gratefully acknowledge the financial support provided by the Slovenian Research Agency (grants P2-0026 and young researcher Amirhossein Lame Jouybari).

REFERENCES

[1] M. Sauzay, K. Bavard, W. Karlsen, ”TEM observations and finite element modelling of channel deformation in pre-irradiated austenitic stainless steels – Interactions with free surfaces and grain boundaries”, Nuclear Materials, Vol. 406, 2010, pp. 152–165.

[2] The MathWorks Inc. (2022). MATLAB version: 9.12.0 (R2022a), Natick, Massachusetts.

[3] A. Marano, Numerical simulation of strain localization in irradiated polycristals, Doctoral dissertation, Université Paris sciences et lettres, 2019.

[4] E. Kroner, Statistical Continuum Mechanics, pringer-Verlag, Wien, 1972.

[5] I. Ramière, T. Helfer, ”Iterative residual-based vector methods to accelerate fixed point iterations, Computers & Mathematics with Applications”, Vol. 70(9), 2015, pp. 2210-2226.

[6] F. Willot, ”Fourier-based schemes for computing the mechanical response of composites with accurate local fields”, Comptes Rendus Mécanique, Vol. 343(3), 2015, pp. 232-245.

[7] R. Quey, P.R. Dawson, F. Barbe, ”Large-scale 3d random polycrystals for the finite element method: generation, meshing and remeshing”, Comput, Methods Appl. Mech. Eng. Vol. 200, 2011, pp. 1729-1745.

[8] Z. Jiao, G.S. Was, ”The role of irradiated microstructure in the localized deformation of austenitic stainless steels”, Nuclear Materials Vol. 407(1), 2010, pp. 34–43.

[9] J. C. Michel, H. Moulinec, P. Suquet, ”Effective properties of composite materials with periodic microstructure: a computational approach”, Computer methods in applied mechanics and engineering, Vol. 172(1-4), 1999, pp. 109-143.

[10] The MathWorks Inc. (2022). Voxview, Natick, Massachusetts: The MathWorks Inc. https://www.mathworks.com/matlabcentral/fileexchange/78745-voxview

APPENDIX

A.1 Notation

The first-order (vector), second-order, and fourth-order tensors are denoted as $\underline{u}$, $\underset{\sim}{A}$, $\underset{\approx}{B}$. The superscripts, ^{tot}, ^{e}, ^{p}, ^{T}, $^{\cdot}$,*, and ^{s}, respectively correspond to the total, elastic, plastic, transpose, time derivative, fluctuation part of tensor field, and variable associated to the slip system. Also, the bar over the tensor field is the spatial mean value over the whole material.

$$\bar{\alpha} = \frac{\sum_{i=1}^{N_{tot}} \alpha_i}{N_{tot}} \tag{A.1}$$

The dot and double dot contractions are denoted as following indices notation (where Einstein summation convention is used).

$$\underline{u}.\underline{v} = u_i v_i \tag{A.2}$$

$$(\underset{\approx}{A} : \underset{\approx}{B})_{ijmn} = A_{ijkl} B_{klmn} \tag{A.3}$$

The fast Fourier transform ($\mathcal{FFT}$) and inverse of fast Fourier transform ($\mathcal{IFFT}$) of a tensor are defined as (in discrete Fourier transform notations),

$$\underset{\sim}{\widehat{B}}(\xi_1, \xi_2, \xi_3) = \mathcal{FFT}\left(\underset{\sim}{B}\right) = \frac{1}{N_{tot}} \sum_{x_1=0}^{N_1-1} \sum_{x_2=0}^{N_2-1} \sum_{x_3=0}^{N_3-1} \underset{\sim}{B}(x_1, x_2, x_3) \exp\left(-2\pi \mathrm{i} \left(\frac{\xi_1 x_1}{N_1} + \frac{\xi_2 x_2}{N_2} + \frac{\xi_3 x_3}{N_3}\right)\right) \tag{A.4}$$

$$\underset{\sim}{B}(x_1, x_2, x_3) = \mathcal{IFFT}\left(\underset{\sim}{\widehat{B}}\right) = \sum_{\xi_1=0}^{N_1-1} \sum_{\xi_2=0}^{N_2-1} \sum_{\xi_3=0}^{N_3-1} \underset{\sim}{\widehat{B}}(\xi_1, \xi_2, \xi_3) \exp\left(2\pi \mathrm{i} \left(\frac{\xi_1 x_1}{N_1} + \frac{\xi_2 x_2}{N_2} + \frac{\xi_3 x_3}{N_3}\right)\right) \tag{A.5}$$

Table 3: Symbols and notation

$\underset{\sim}{\varepsilon}^{tot}$	Total imposing linear strain tensor	$\underset{\sim}{\sigma}$	Cauchy stress tensor
$\underset{\approx}{\Lambda}$	Elasticity tensor	τ^{s}	Resolved shear stress
$\underline{m}^{\mathsf{s}}$	Slip direction	$\underline{n}^{\mathsf{s}}$	normal to slip plan
$\otimes$	Tensor product	$\underset{\sim}{\mu}^{\mathsf{s}}$	$= \underline{m}^{\mathsf{s}} \otimes \underline{n}^{\mathsf{s}}$
sym	Symmetric part of tensor	γ^{s}	Shear strain
$\dot{\gamma}^{\mathsf{s}}$	Shear strain rate	τ^{s}_{cr}	Critical resolved shear stress
exp	Exponential function	$\gamma^{\mathsf{s}}_{\mathsf{cum}}$	Cumulative shear strain
t	Time	sign	sign function
$\underline{x}$	Position of material point	$\mathcal{B}$	Whole material
$\partial\mathcal{B}$	Boundary of material	$\underline{n}$	Normal vector
#	Periodic	$-$#	Anti-periodic
div	Divergence operator	$*$	Convolution integral
τ	Polarization tensor field	$\underset{\approx}{I}^{(1)}$	$= \frac{1}{2}\left(\delta_{ik}\delta_{jl} + \delta_{il}\delta_{jk}\right)$
$\underset{\approx}{\Lambda}^{h}$	Homogeneous isotropic elasticity tensor	$\underline{\xi}$	Frequency in Fourier space
$\forall$	For all	δ_{ij}	Kronecker delta
$\nabla\underline{u}$	Displacement gradient tensor	$\underset{\sim}{1}$	Second order identity tensor
$\langle\rangle$	Macaulay brackets	$\underset{\approx}{\Gamma}^{\mathsf{M}}$	Modified Green operator
p	Effective cumulative plastic deformation	$\underline{\mathfrak{f}}$	Modified frequency vector in Fourier space
θ	Rotation angel	arccos	Inverse of cos
tr	Trace operator	L^{p}	Plastic part of velocity gradient tensor
$\mathcal{H}$	Heaviside step function	$\underset{\sim}{U}^{\mathsf{e}}$	Stretch tensor
R	Rotation tensor	N_{tot}	Total number of voxels
$\underset{\sim}{L}_i$	Length of material on i-direction	i	Imaginary number

A.2 Time integration

The time integration algorithm consists of finding the increments of state variables ($\Delta v^{\mathsf{i+1}}$) by evaluating residual and Jacobian ($\mathcal{J}^{\mathsf{i}},\ R^{\mathsf{i}}$) of the respected variables at the previous iteration and updating the state variables, $v^{\mathsf{i+1}}$, until reaching the tolerance.

$$\begin{cases} \mathcal{J}^{\mathsf{i}}(v^{\mathsf{i}}).\Delta v^{\mathsf{i+1}} = -R^{\mathsf{i}}(v^{\mathsf{i}}) \\ v^{\mathsf{i+1}} = v^{\mathsf{i}} + \Delta v^{\mathsf{i+1}} \end{cases} \tag{A.6}$$

We assume that the state variables at the previous time step and the total strain field at the current time step are known. The residual and their partial derivatives are derived as:

$$R_{\underset{\sim}{\varepsilon}^{\mathsf{e}}} = \Delta\underset{\sim}{\varepsilon}^{\mathsf{e}} + \underset{\sim}{\varepsilon}^{\mathsf{e}}(t_n) - \underset{\sim}{\varepsilon}^{\mathsf{tot}}(t_n + \Delta t) + \underset{\sim}{\varepsilon}^{\mathsf{p}}(t_n) + \sum_s \Delta\gamma^s \mathsf{sym}(\underset{\sim}{\mu}^{\mathsf{s}}) \tag{A.7}$$

$$R_{\gamma^s} = \Delta\gamma^s - \Delta t\ \mathsf{sign}(\tau^{\mathsf{s}}) \left\langle \frac{|\tau^{\mathsf{s}}| - \tau^{\mathsf{s}}_{\mathsf{cr}}}{k} \right\rangle^{\mathsf{n}} \tag{A.8}$$

$$\frac{\partial R_{\underset{\sim}{\varepsilon}^{\mathsf{e}}}}{\partial \Delta\underset{\sim}{\varepsilon}^{\mathsf{e}}} = \underset{\approx}{I}^{(1)} \tag{A.9}$$

$$\frac{\partial R_{\underset{\sim}{\varepsilon}^{\mathsf{e}}}}{\partial \Delta\gamma^j} = \mathsf{sym}\left(\underset{\sim}{\mu}^{\mathsf{j}}\right) \tag{A.10}$$

$$\frac{\partial R_{\gamma^{\mathsf{s}}}}{\partial \Delta\underset{\sim}{\varepsilon}^{\mathsf{e}}} = -\Delta t \frac{n}{k} \left\langle \frac{|\tau^{\mathsf{s}}| - \tau^{\mathsf{s}}_{\mathsf{cr}}}{k} \right\rangle^{\mathsf{n\text{-}1}} \mathsf{sym}\left(\underset{\sim}{\mu}^{\mathsf{j}}\right) : \underset{\approx}{\Lambda} \tag{A.11}$$

$$\frac{\partial R_{\gamma^{\mathsf{s}}}}{\partial \Delta\gamma^{\mathsf{s}}} = \delta_{sj} \left(1 + \Delta t\ \mathsf{sign}\left(\tau^{\mathsf{s}}\gamma^{\mathsf{j}}\right) \frac{n}{k} \left\langle \frac{|\tau^{\mathsf{s}}| - \tau^{\mathsf{s}}_{\mathsf{cr}}}{k} \right\rangle^{\mathsf{n\text{-}1}} \left[H^{\mathsf{s}} - \frac{\Delta\tau^{\mathsf{s}} \exp\left(-\frac{\gamma^{\mathsf{s}}_{\mathsf{cum}}}{\gamma^{\mathsf{s}}_0}\right)}{\gamma^{\mathsf{s}}_0} \right] \right) \tag{A.12}$$